

Pyrochlore phase in the $\text{Bi}_2\text{O}_3\text{--Fe}_2\text{O}_3\text{--WO}_3\text{--(H}_2\text{O)}$ system: its stability field in the low-temperature region of the phase diagram and thermal stability

Makariy S. Lomakin^{1,2,a}, Olga V. Proskurina^{1,3,b}, Aleksandr A. Levin^{1,c}, Vladimir N. Nevedomskiy^{1,d}

¹Ioffe Institute, St. Petersburg, Russia

²St. Petersburg Electrotechnical University “LETI”, St. Petersburg, Russia

³St. Petersburg State Institute of Technology, St. Petersburg, Russia

^alomakinmakariy@gmail.com, ^bproskurinaov@mail.ru, ^caleksandr.a.levin@mail.ioffe.ru, ^dnevedom@mail.ioffe.ru

Corresponding author: M. S. Lomakin, lomakinmakariy@gmail.com

ABSTRACT The concentration stability field localization of the pyrochlore-structured compounds of variable composition formed in the $\text{Bi}_2\text{O}_3\text{--Fe}_2\text{O}_3\text{--WO}_3$ system under hydrothermal conditions at a temperature of $T = 200^\circ\text{C}$ and a pressure of $P = 7$ MPa was determined. It was found that the pyrochlore-structured compounds stability field is longitudinally limited within the atomic ratios $0.47 < \text{Bi}/\text{W} < 1.25$, and in the transverse direction within $1.14 < \text{Bi}/\text{Fe} < 1.87$. It was shown that the pyrochlore phase cubic unit cell parameter a depends on the compound chemical composition as follows: it increases linearly from ~ 10.3319 Å to ~ 10.4199 Å with an increase in the Bi/W atomic ratio from ~ 0.47 to ~ 1.25 . It was established that from the $\text{Bi}_2\text{O}_3\text{--WO}_3$ system side, there is a region of two-phase equilibrium, in which a pyrochlore phase of variable composition coexists with the Bi_2WO_6 compound, which is formed in the form of plate-like (thickness $h \sim 50\text{--}100$ nm) nanoparticles. It was shown that from the $\text{Bi}_2\text{O}_3\text{--Fe}_2\text{O}_3$ system side, there is a region of compositions, in which the pyrochlore phase of the most enriched in bismuth oxide composition coexists with the Bi_2WO_6 compound, which is formed in the form of rod-shaped ($h \sim 10\text{--}30$ nm) nanoparticles, and with the X-ray amorphous phase composition, formed in the form of nanocrystalline particles about 10 nm in size. It was found that the higher temperature point of the pyrochlore-structured compounds stability field does not exceed 725°C , which allows them to be synthesized only by “soft chemistry” methods.

KEYWORDS pyrochlore-structured phase, hydrothermal synthesis, crystal structure, phase diagram, thermal stability

ACKNOWLEDGEMENTS XRD, SEM and EDXMA studies were performed employing the equipment of the Engineering Center of the St. Petersburg State Institute of Technology (Technical University). TEM studies and the analysis of XRD data have been carried out using the equipment and software of the Joint Research Center “Materials science and characterization in advanced technology” (Ioffe Institute). DSC/TG studies were performed employing the equipment of the First All-Russian Engineering Center for Molecular Layering Technology (St. Petersburg State Institute of Technology (Technical University)). HTXRD studies have been carried out using the equipment of the Center for X-Ray Diffraction Studies of the Research Park of St. Petersburg State University.

The authors express their deep gratitude to Corr. Mem. RAS Victor Vladimirovich Gusarov for valuable comments and advice on improving the quality of the manuscript.

The work was financially supported by the Russian Science Foundation (Project No. 20-63-47016).

FOR CITATION Lomakin M.S., Proskurina O.V., Levin A.A., Nevedomskiy V.N. Pyrochlore phase in the $\text{Bi}_2\text{O}_3\text{--Fe}_2\text{O}_3\text{--WO}_3\text{--(H}_2\text{O)}$ system: its stability field in the low-temperature region of the phase diagram and thermal stability. *Nanosystems: Phys. Chem. Math.*, 2024, **15** (2), 240–254.

1. Introduction

The pyrochlore-structured complex oxide compounds attract the researchers active attention because they have a set of interesting physicochemical properties for investigation, in particular, magnetic [1–5], dielectric [3, 5–7], transport [8, 9], photocatalytic [10–12]. Due to this, they can be considered as promising materials for the manufacture of coatings, for example, parts of gas turbines operating at elevated temperatures [13], as well as ion-exchange materials for the immobilization of radioactive waste [14]. The pyrochlore-structured compounds are characterized by a large isomorphic capacity, which determines the existence of this structural type in both binary [14–16] and more multicomponent oxide systems [1–11]. In most oxide systems, the pyrochlore-structured compounds are obtained from simple oxides by the solid-state synthesis, since, as a rule, this structural type is quite stable at elevated temperatures [17, 18]. Despite this, the application of “soft chemistry” methods, in particular, the hydrothermal method, opens up opportunities for studying

phase transformations involving the pyrochlore phase, occurring in the low-temperature region of phase diagrams [19–23]. It should be noted that, as a rule, complex oxide phases of variable composition are characterized by a narrowing of the equilibrium concentration boundaries of the stability field with increasing synthesis temperature, that is, when moving towards the melting or solid-phase decomposition temperature. Reducing the synthesis temperature of such compounds, on the contrary, leads to the possibility of widely varying their quantitative composition and, as a consequence, properties, while remaining within their stability field boundaries. It should be mentioned that when investigating phase transformations occurring in the low-temperature region of the phase diagram, it is also interesting to study the thermal stability of oxide compounds formed during hydrothermal synthesis.

Phase equilibria in the $\text{Bi}_2\text{O}_3\text{--Fe}_2\text{O}_3\text{--WO}_3$ system have not previously been the subject of systematic research, since only a few works devoted to the synthesis and characterization of compounds formed in this system are found in the scientific literature [24–26]. In particular, pyrochlore-structured compounds of variable composition were for the first time obtained and structurally characterized in a recent work by the authors [27] in 2020; however, studies of their stability field localization, as well as their thermal stability, have not been carried out to date.

The aim of this work is to determine the localization of the concentration and temperature stability fields of pyrochlore-structured compounds of variable composition in the $\text{Bi}_2\text{O}_3\text{--Fe}_2\text{O}_3\text{--WO}_3$ system.

2. Materials and Methods

2.1. Synthesis section

The synthesis procedure, which is the same for all samples, is described below. Table 1 shows the molar amounts of reagents (x , y , z) and the measured values of the precursor suspension pH corresponding to the various samples. To obtain a sample, x mmol of crystalline hydrate of bismuth (III) nitrate, $\text{Bi}(\text{NO}_3)_3 \cdot 5\text{H}_2\text{O}$ (puriss. spec.), and y mmol of crystalline hydrate of iron (III) nitrate, $\text{Fe}(\text{NO}_3)_3 \cdot 9\text{H}_2\text{O}$ (pur.), were dissolved in q ml of 6 M HNO_3 (puriss. spec.), after which h ml of distilled water was added to the resulting solution. Next, z mmol of sodium tungstate (VI) crystalline hydrate, $\text{Na}_2\text{WO}_4 \cdot 2\text{H}_2\text{O}$ (puriss. spec.), was dissolved in g ml of distilled water and the resulting solution was added dropwise into the acidic solution of bismuth and iron nitrates stirred with a magnetic stirrer at 800 rpm (~ 30 mL of distilled water was then added there and used to rinse the beaker that had contained the sodium tungstate solution). After stirring the obtained suspension for 1 h, a solution of 2 M NaOH was added to it dropwise until reaching pH of $\sim 4\text{--}5$ (Table 1). The amorphous precursor suspension obtained this way, was additionally stirred at 1000 rpm for ~ 1 h and then transferred into Teflon chambers ($\sim 80\%$ filling) and placed in steel autoclaves, which were then put in a furnace heated up to $T = 200^\circ\text{C}$. After 72 h, the autoclaves were removed from the furnace and cooled in air. The resulting precipitates were separated from the mother liquor (it was poured out), rinsed with distilled water several times by decantation and dried at 80°C for 24 h.

2.2. Characterization

The crystal structure of the samples synthesized via a hydrothermal method was analyzed by X-ray diffraction (XRD) using a Rigaku SmartLab 3 Powder X-ray Diffractometer (Rigaku Corporation, Japan). XRD patterns ($\text{Co-}K_\alpha$ radiation (average wavelength $\lambda = 1.79028 \text{ \AA}$) of an X-ray tube with a cobalt anode filtered using a $\text{Fe } K_\beta$ filter) were recorded in the Bragg-Brentano geometry at room temperature. The measurements were carried out in the symmetrical $\theta\text{--}2\theta$ mode (θ is the angle of incidence of the X-ray beam on the surface of the sample, 2θ is the diffraction angle). The recording of XRD patterns was carried out using a one-dimensional (1D) silicon strip detector D/teX Ultra 250. The measurements were carried out in the range of angles $2\theta = 10^\circ\text{--}80^\circ$ with a step of $\Delta 2\theta = 0.02^\circ$, and the total time at the point was 123 seconds (conversion from the used linear detector to a point detector).

The XRD pattern of the sample 5.12 was also obtained on the same diffractometer using a $\text{Cu-}K_\alpha$ radiation (average wavelength $\lambda = 1.54186 \text{ \AA}$) after an X-ray tube with a copper anode and a $\text{Ni } K_\beta$ filter. This measurement was carried out in the range of angles $2\theta = 6^\circ\text{--}140^\circ$ with a step of $\Delta 2\theta = 0.01^\circ$, and the total time at the point was 2560 seconds. Thus obtained XRD pattern was used to carry out the precise calculations of unit cell parameters, average crystallite size and microstrains.

High-temperature XRD (HTXRD) studies were carried out using a Rigaku Ultima IV Powder X-ray Diffractometer (Rigaku Corporation, Japan), equipped with a 1D silicon strip detector D/teX Ultra 250 and a high-temperature camera SHT-1500 (Rigaku Corporation, Japan). The XRD patterns were recorded using a $\text{Cu-}K_\alpha$ radiation of an X-ray tube with a copper anode filtered with a $\text{Ni } K_\beta$ filter (average wavelength $\lambda = 1.54186 \text{ \AA}$) in the range of angles $2\theta = 10^\circ\text{--}80^\circ$ with a step of $\Delta 2\theta = 0.02^\circ$, and the speed was $4^\circ/\text{min}$. The measurements were performed in air in the temperature range from 25°C to 585°C (step was 40°C) and in the range $585\text{--}785^\circ\text{C}$ (step was 20°C), heating rate between temperature points was $10^\circ\text{C}/\text{min}$, exposure at temperature before XRD recording was 20 minutes. The sample was prepared by deposition from an alcohol suspension onto a standard platinum substrate. The temperature was controlled using a Pt-Rh thermocouple located in close proximity to the substrate. Before the experiment, the positions of the diffraction angles were corrected using an external silicon standard.

TABLE 1. Sample names and synthesis parameters

Sample	n(Bi) (<i>x</i>), mmol	n(Fe) (<i>y</i>), mmol	n(W) (<i>z</i>), mmol	Bi ³⁺ and Fe ³⁺ nitrates solution		Sodium WO ₄ ²⁻ solution	Precursor suspension <i>pH</i>
				Vol.* of 6 M HNO ₃ (<i>q</i>), ml	Vol.* of distilled water (<i>h</i>), ml	Vol.* of distilled water (<i>g</i>), ml	
				5.3	2.779	2.799	4.242
5.6	2.012	1.791	5.777	4.8	23.9	41.3	4.50
5.8	2.744	2.340	4.313	6.5	32.7	30.8	4.77
5.9	3.096	2.620	3.609	7.4	36.9	25.8	5.03
5.12	2.010	1.386	5.781	4.8	23.9	41.3	4.55
5.16	3.388	2.432	3.025	8.1	40.3	21.6	4.88
5.17	3.717	2.682	2.367	8.8	44.2	16.9	4.48
5.18	4.040	2.928	1.720	9.6	48.1	12.3	4.58
5.20	2.354	1.273	5.092	5.6	28.0	36.4	4.58
5.21	2.688	1.530	4.425	6.4	32.0	31.6	4.57
5.22	3.015	1.782	3.769	7.2	35.9	26.9	4.42
5.34	4.186	2.360	1.427	10.0	49.8	10.2	4.69

*Volume

The crystal structure of the annealed samples was analyzed by XRD using an X-ray powder diffractometer DRON-8N (IC "Burevestnik", Russia) in the Bragg-Brentano geometry (an X-ray tube with copper anode, Ni K_{β} filter, Cu- K_{α} radiation (average wavelength $\lambda = 1.54186 \text{ \AA}$)), equipped with a position-sensitive (PSD) linear detector Mythen2 R 1D (DECTRIS Ltd., Switzerland) with an opening angle of 4.48° and with a single parabolically bent Göbel Mirror placed in the beam path so the line focus of the X-ray source. The measurements were carried out in the range of angles $2\theta = 10^{\circ} - 80^{\circ}$ with a step of $\Delta 2\theta = 0.0142^{\circ}$, and the total time at the point was 180 seconds.

The preprocessing of the measured XRD patterns of samples in order to obtain the parameters of the observed XRD reflections necessary for unit cell and microstructure calculations was carried out using the EVA program, version 5.1.0.5 (Bruker AXS, Germany). To increase the precision of the analysis, the observed values of the Bragg angles obtained by EVA were corrected for zero shift and displacement (see [28] for details). Angular corrections (zero shift and displacement) were obtained by the external standard method based on additional measurements of a 5.12 powder sample mixed with NaCl powder, which was calibrated by the internal standard method using the Si640f powder XRD standard (NIST, USA).

X-ray phase analysis (XPA) of the measured XRD patterns of samples was carried out using the Crystallographica Search-Match program, version 3.1.0.2 (Oxford Cryosystems Ltd., England) using the Powder Diffraction File-2 (PDF-2) [29] and Cambridge Structural Database (CSD) (<https://www.ccdc.cam.ac.uk/structures/>).

Scanning electron microscopy (SEM) images and bulk elemental composition of the samples were obtained on a Tescan Vega 3 SBH scanning electron microscope (Tescan Orsay Holding, Czech Republic) with an Oxford Instruments Energy Dispersive X-ray Microanalysis (EDXMA) attachment. The relative number of elements was calculated using the AZtec software. The characteristic emission spectra of each sample were accumulated from four sites with a total area of $\sim 9 \text{ mm}^2$, with a set of statistics for at least 2 million pulses at each site. The readings from each site were averaged, and the measurement error was determined at a confidence level of 0.95.

In transmission electron microscopy (TEM) studies a JEM-2100F microscope at an accelerating voltage of 200 kV is employed. Specimens from the samples were prepared by one of the traditional methods, that is, by dispersing a suspension of a weighed portion of powder in ethanol by ultrasound for 8–10 min, followed by precipitation and drying on a thin supporting carbon film.

The thermal behavior of the sample 5.16 was studied by differential scanning calorimetry (DSC) together with thermogravimetry (TG) when heating the sample in an open platinum crucible in the temperature range $30 - 900^{\circ}\text{C}$ in a

dynamic argon atmosphere (flow rate 50 ml/min) with a heating rate of $10^\circ\text{C}/\text{min}$ on a synchronous thermal analyzer Netzsch STA 449 F5 Jupiter.

3. Results and discussions

3.1. Chemical composition

The EDXMA data on the bulk chemical composition of the samples are presented in Table 2 in the form of atomic ratios and in Fig. 1 (a – nominal composition specified for the synthesis, b – bulk chemical composition) as points on the concentration triangle of the $\text{BiO}_{1.5}\text{-FeO}_{1.5}\text{-WO}_3$ system.

TABLE 2. Bulk chemical composition of samples synthesized by the hydrothermal method, in rel. at. units, according to the EDXMA data

Example	Bi/W $\pm\Delta$		Fe/W $\pm\Delta$		Bi/Fe $\pm\Delta$	
	Nom.*	Bulk	Nom.*	Bulk	Nom.*	Bulk
5.3	0.66	0.57 ± 0.05	0.66	0.50 ± 0.02	1.00	1.14 ± 0.13
5.6	0.35	0.47 ± 0.04	0.31	0.36 ± 0.02	1.13	1.30 ± 0.10
5.8	0.64	0.55 ± 0.03	0.54	0.44 ± 0.01	1.19	1.24 ± 0.05
5.9	0.86	0.79 ± 0.07	0.73	0.56 ± 0.01	1.18	1.41 ± 0.13
5.12	0.35	0.52 ± 0.03	0.24	0.28 ± 0.01	1.46	1.85 ± 0.07
5.16	1.12	1.05 ± 0.10	0.80	0.70 ± 0.02	1.40	1.49 ± 0.11
5.17	1.57	1.45 ± 0.04	1.13	0.81 ± 0.03	1.39	1.78 ± 0.07
5.18	2.35	2.09 ± 0.07	1.70	1.27 ± 0.02	1.38	1.65 ± 0.04
5.20	0.46	0.47 ± 0.03	0.25	0.25 ± 0.02	1.84	1.87 ± 0.09
5.21	0.61	0.54 ± 0.04	0.35	0.32 ± 0.01	1.74	1.71 ± 0.12
5.22	0.80	0.74 ± 0.05	0.47	0.44 ± 0.02	1.70	1.69 ± 0.12
5.34	2.93	2.41 ± 0.11	1.65	1.49 ± 0.04	1.78	1.62 ± 0.04

*Nominal composition specified for the synthesis

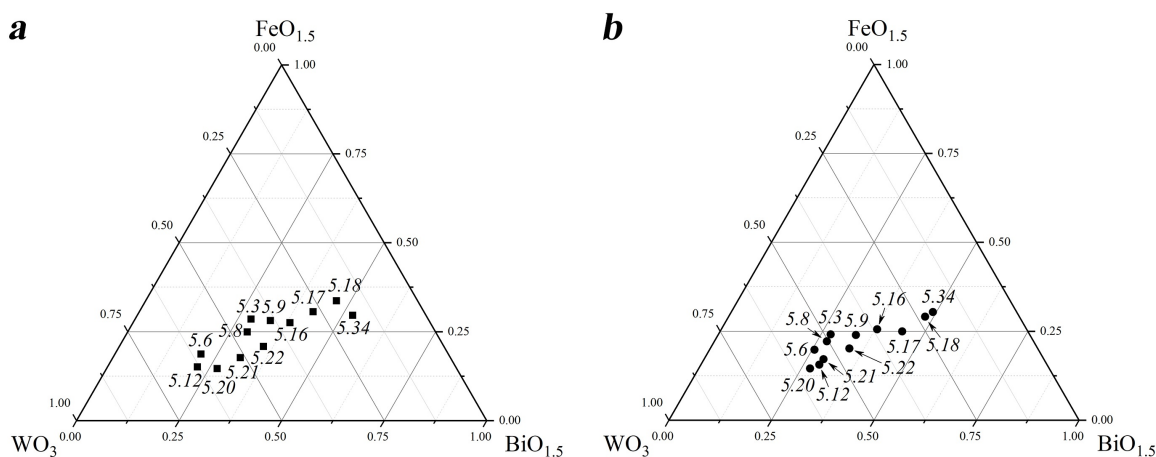


FIG. 1. (a) Nominal and (b) bulk (according to the EDXMA data) chemical composition of samples synthesized by the hydrothermal method on the concentration triangle of the $\text{BiO}_{1.5}\text{-FeO}_{1.5}\text{-WO}_3$ system

It should be noted that only for samples 5.20, 5.21, 5.22 and 5.34, there is a good agreement between their bulk and nominal compositions. For samples 5.6 and 5.12, depletion of their bulk compositions by tungsten oxide is observed, and for samples 5.3, 5.8, 5.9, 5.16, 5.17 and 5.18 – by iron oxide, relative to their corresponding nominal compositions. The

indicated depletion of the bulk composition for any component is due to the fact that some part of the components may not insert the solid phase of the hydrothermal synthesis product and remains dissolved in the cooled hydrothermal fluid, after which it will be removed from the system when rinsing the resulting precipitates.

3.2. XRD analysis

Powder X-ray diffraction patterns of samples synthesized by the hydrothermal method are shown in Fig. 2. In samples 5.3, 5.6, 5.8, 5.9 and 5.16 (Fig. 2a), only crystalline compounds with a pyrochlore structure of variable composition (CSD 1961005) were found. However, in the case of sample 5.3, when rinsing the precipitate obtained as a result of hydrothermal synthesis by decantation, it was noticed that the poured out liquid is cloudy and contains suspended particles. After drying the suspension, when studying these particles on SEM, it was found that their chemical composition was enriched with iron. Apparently, the nominal composition of sample 5.3 is beyond the stability field boundary of the pyrochlore phase from the Fe_2O_3 side, therefore, part of the iron (III) oxide does not insert into the pyrochlore phase structure and forms an impurity phase. Crystallization of iron (III) oxide, which is excessive in relation to the pyrochlore phase composition, in a slightly acidic medium of a hydrothermal fluid ($\text{pH} \sim 4\text{--}5$), is apparently difficult, since after 72 h of isothermal exposure ($T = 200^\circ\text{C}$), it is impossible to observe reflections related to any structural modifications of iron (III) oxide in the XRD pattern of the sample 5.3. It is possible to significantly accelerate the crystallization of excess iron (III) oxide by lowering the hydrothermal fluid pH to strongly acidic values ($\text{pH} < 1$), which is shown in [19, 27], where pyrochlore/ $\alpha\text{-Fe}_2\text{O}_3$ composites are obtained.

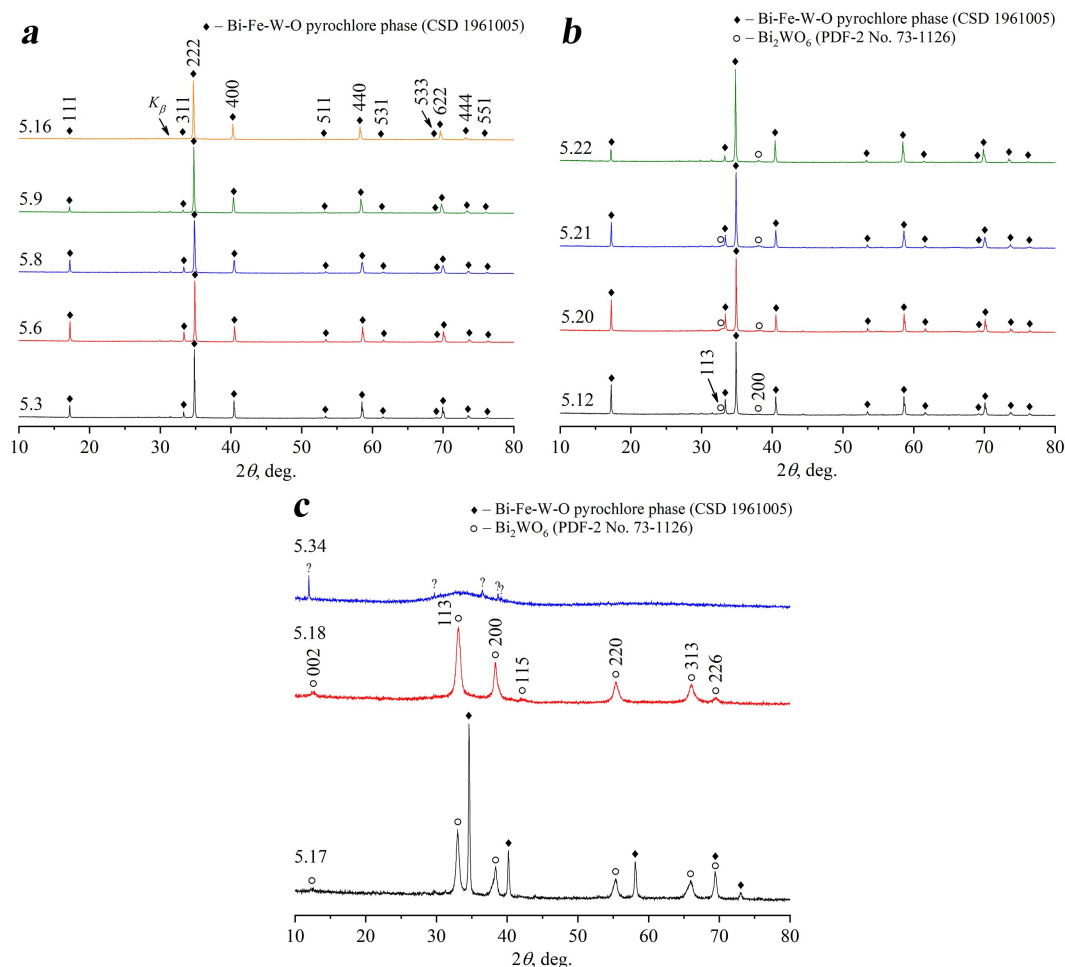


FIG. 2. Powder XRD patterns of samples synthesized by the hydrothermal method: (a) samples 5.3, 5.6, 5.8, 5.9, 5.16; (b) samples 5.12, 5.20, 5.21, 5.22; (c) samples 5.17, 5.18, 5.34 (Co- K_α radiation) (Miller indices hkl are indicated only for selected reflections)

XRD patterns of samples 5.12, 5.20, 5.21, and 5.22 (Fig. 2b) show, in addition to intense reflections of the pyrochlore phase, a set of barely noticeable reflections, identical for all these samples and related to the compound Bi_2WO_6 (PDF-2 No. 73-1126), crystallizing in the structural type of the Aurivillius phase. As a result of the pyrochlore-structured compounds composition study in these samples by the local EDXMA of single particles, it was found that the compositions determined in this way do not differ from the bulk compositions of the corresponding samples within the limits of estimated standard deviations (e.s.d.s). At the same time, the local EDXMA of single Aurivillius phase particles in these

samples showed that there is no iron in their composition, which indicates namely the formation of a two-component Aurivillius phase. Thus, it can be assumed that the bulk composition of the obtained two-phase samples, in which the Bi_2WO_6 phase is present in an impurity amount and does not affect the results of the EDXMA, with some approximation corresponds to the stability field boundary of the pyrochlore phase from the side of the Bi_2WO_6 phase.

First, the precise value of the cubic unit cell parameter of pyrochlore ($a = 10.33193(8)$ Å) was calculated for sample 5.12 using program Celsiz, version 1.1 [30] working by the least squares method and using the Miller indices hkl of all observed pyrochlore reflections and their Bragg angles $2\theta_B$ after applying the angular corrections (to zero shift and displacement). For these calculations, the XRD pattern of sample 5.12, measured with $\text{Cu-}K_\alpha$ radiation and a long intensity accumulation total time in step (2560 s) was used. Note that without taking into account angular corrections, the value of a is $\sim 0.0035\%$ higher and its e.s.d. is ~ 1.5 times greater.

Further, using the same XRD pattern of sample 5.12, measured with high statistics, which is described above, estimates were made of the average size D of coherent X-ray scattering regions, also called crystallites, and the absolute value of the average microdeformation (microstrain) ε_s in these regions. To obtain these parameters D and ε_s of the microstructure, using the SizeCr program [31], a profile analysis of XRD lines (line profile analysis, LPA) was carried out utilizing the Williamson-Hall (WHP) [32] and size-strain plot (SSP) [33] graphical methods.

According to the value of the criterion (full width at half the maximum intensity) $FWHM/B_{int} = 0.70(5)$, averaged over all observed XRD reflections, where $FWHM$ is the observed $FWHM$ of the XRD reflection, and $B_{int} = \frac{I_{int}}{I_{max}}$ is its integral width (I_{int} and I_{max} are integral and maximum reflection intensities, respectively), the observed reflections of sample 5.12 are characterized by a pseudo-Voigt (pV) type [34]. The observed values of the $FWHM$ were corrected for instrumental broadening (hereinafter the corrected $FWHM$ referred to as $FWHM_{corr}$) using the SizeCr program adopting procedures that take into account the type of XRD reflections [31–33]. Also, taking into account the type of XRD reflections, the program SizeCr calculates the points of the WHP and SSP graphs using the corrected values, $FWHM_{corr}$ and $2\theta_B$. The coefficients $K_{Scherrer} = 0.94$ in the Scherrer equation [35] and $K_{strain} = 4$ in the Wilson-Stokes equation [36] were used in the calculations, relating the contributions to the broadening of reflections with the values D and ε_s , respectively. When constructing the WHP and SSP graphs, the coefficient of determination R_{cod} was calculated (see its definition in [31, 33]), showing how well the experimental points fit on the approximation line $Y = A + B \cdot X$ (ideally, when all points fit on the line, $R_{cod} = 100\%$).

Fig. 3 shows the obtained SSP and WHP graphs for sample 5.12.

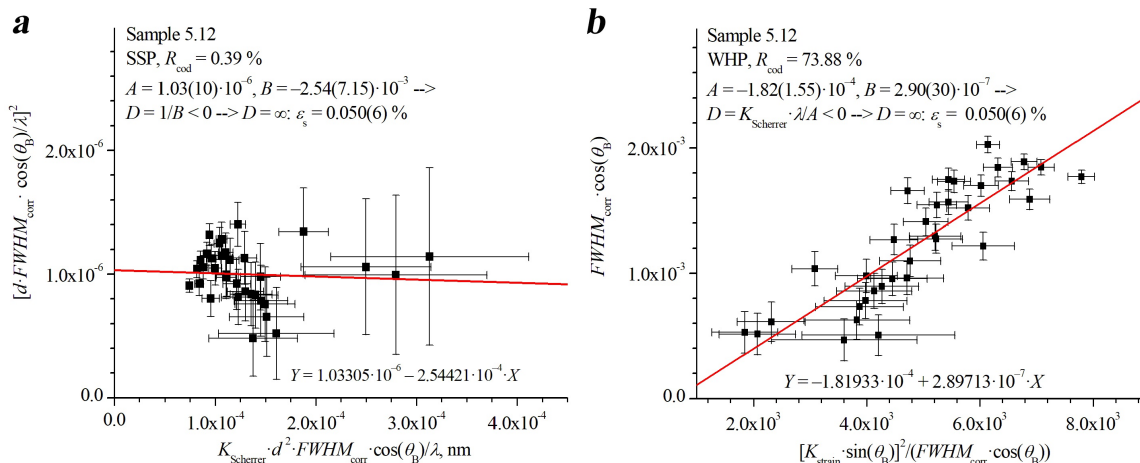


FIG. 3. (a) SSP and (b) WHP graphs constructed using XRD line profile analysis performed for sample 5.12. Approximation straight line $Y = A + B \cdot X$ of SSP (and WHP) dependence is shown in the corresponding Figures, where the values Y and X are indicated along the ordinate and abscissa axes, respectively. The symbol d means the interplanar distance corresponding to the reflection with Miller indices hkl and Bragg angle $2\theta_B$ (Bragg angle corrections are applied), and $\lambda = 1.540598$ Å is the wavelength of $\text{Cu-}K_{\alpha 1}$ radiation (after correcting the contribution of $\text{Cu-}K_{\alpha 2}$).

For sample 5.12, SSP shows low reliability, which is reflected by a large spread of points around the approximation line and a low value of the coefficient $R_{cod} = 0.39\%$ (Fig. 3a). At the same time, the WHP method for sample 5.12 (Fig. 3b) is characterized by a sufficiently large value $R_{cod} = 73.88\%$. Nevertheless, both methods give one the same results, indicating large crystallite sizes and confirming each other. In particular, as can be seen from Fig. 3a,b, the approximation straight line $Y = A + B \cdot X$ for sample 5.12 in the case of SSP is characterized by a negative slope ($B < 0$), and in the case of WHP its intersection with the Y axis occurs in the region of negative values ($A < 0$). In both cases, this formally corresponds to the infinite size of the crystallites ($D = \infty$). In the case of $D = \infty$, the values ε_s^{hkl} of

the microstrain corresponding to each observed reflection with Miller hkl indices were calculated by the SizeCr program from the Wilson-Stokes equation [36]. Indeed, for sample 5.12, the dependence $\varepsilon_s^{hkl}(2\theta_B)$ shows an almost uniform distribution of experimental ε_s^{hkl} values around the mean value $\varepsilon_s = 0.050(6)\%$ obtained by root-mean-square averaging (Fig. 4).

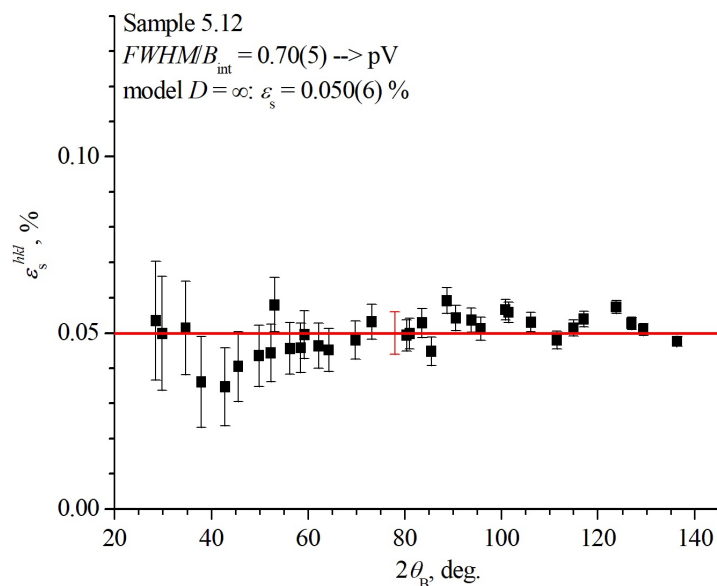


FIG. 4. Distribution of microstrain values ε_s^{hkl} along the Bragg angles $2\theta_B$. The ε_s^{hkl} values are calculated for reflections hkl within the framework of the $D = \infty$ model. The horizontal line corresponds to the mean value ε_s obtained by the root-mean-square averaging of the ε_s^{hkl} values

Taking into account that the observed values of the $FWHM$ of the pyrochlore phase reflections in other samples differ only slightly from those in sample 5.12, there is no reason to expect significant differences in the calculated values of the average crystallite sizes and microstrains for the crystalline pyrochlore phase in other synthesized samples.

Fig. 5 shows the dependence of the pyrochlore phase cubic unit cell parameter a on the phase composition expressed in Bi/W (at.) atomic ratio and assumed to be equal to the bulk composition of the samples 5.3, 5.6, 5.8, 5.9, 5.16, 5.12, 5.20, 5.21, and 5.22. The unit cell parameter a of these samples was calculated in the Celsiz program in the same way as described above for sample 5.12, based on the results obtained from the analysis of their XRD patterns measured with Co- K_α radiation and total time of 123 s of the intensity accumulation in point step (except for sample 5.12, for which the precise parameter a value was used, obtained as described above). According to the data presented in Fig. 5, the unit cell parameter increases linearly with an increase in the atomic ratio Bi/W, which, apparently, is due to an increase in the number of Bi^{3+} cations having a large radius in the structure due to their occupation of cation vacancies in the A_2O' sublattice.

In the XRD pattern of the sample 5.17 (Fig. 2c), reflections of the pyrochlore phase are detected, the unit cell parameter of which is $a = 10.4199(6)$ Å. The pyrochlore phase composition in this sample corresponds to the pyrochlore phase stability field boundary from the Bi_2O_3 - Fe_2O_3 system side and can be indirectly determined through the unit cell parameter when it is substituted into the equation $a = f(\text{Bi}/\text{W}, \text{at.})$ shown in Fig. 5: determined in this way Bi/W atomic ratio is ~ 1.25 .

In addition to the pyrochlore phase reflections, a set of reflections is observed in sample 5.17, which can be equally attributed to both the compound Bi_2WO_6 (PDF-2 No. 73-1126) and the compound of the formal composition $\text{Bi}_{1.5}\text{Fe}_{0.5}\text{WO}_6$ (PDF-2 No. 38-1285). The same set of reflections is observed in the XRD pattern of sample 5.18, while the pyrochlore phase reflections are absent (Fig. 2c). Both compounds (Bi_2WO_6 and $\text{Bi}_{1.5}\text{Fe}_{0.5}\text{WO}_6$) belong to the class of Aurivillius phases and have the same set of reflections, apparently differing in the number and nature of perovskite-like layers. It is extremely difficult to distinguish these compounds in XRD patterns, which requires the use of additional research methods, in particular, the analysis of these compounds particles chemical composition by the local EDXMA. In samples 5.17 and 5.18, it was not possible to carry out such an analysis (see Section 3.3), as was done for other samples described above. However, TEM studies confirmed the formation of a single-layer Aurivillius phase Bi_2WO_6 in them. In sample 5.17 the Aurivillius phase Bi_2WO_6 crystallite size in the crystallographic direction [113] was calculated using the Scherrer method and amounted to ~ 20 nm. Two amorphous halos are observed in the XRD pattern of sample 5.34 (Fig. 2c), against which narrow but low-intensity reflections of an unknown phase are visible.

When comparing the chemical composition of samples 5.17, 5.18, and 5.34 with the results of XRD, it can be concluded that they contain a phase, which chemical composition enriched in bismuth and iron oxides and the reflections

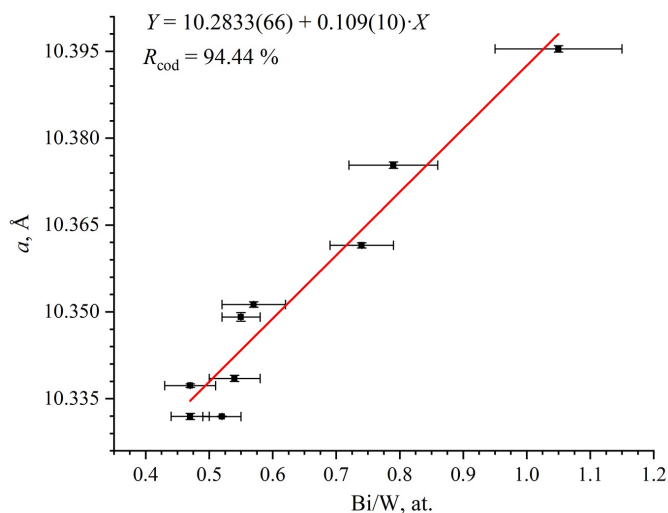


FIG. 5. Dependence of the pyrochlore phase cubic unit cell parameter a on the phase composition expressed in Bi/W (at.) atomic ratio and assumed to be equal to the bulk composition of the samples 5.3, 5.6, 5.8, 5.9, 5.16, 5.12, 5.20, 5.21, and 5.22

of which cannot be detected in XRD patterns, and the amount of this phase increases with an increase in the content of these oxides in the bulk chemical composition of the samples.

Fig. 6 shows a concentration triangle, which compares the results of determining the bulk chemical and phase composition of the obtained samples. The shaded area indicates the localization of the pyrochlore-structured compounds concentration stability field in the $\text{BiO}_{1.5}\text{-FeO}_{1.5}\text{-WO}_3$ system at $T = 200^\circ\text{C}$, which is longitudinally limited within the atomic ratios $0.47 < \text{Bi}/\text{W} < 1.25$, and in the transverse direction within $1.14 < \text{Bi}/\text{Fe} < 1.87$.

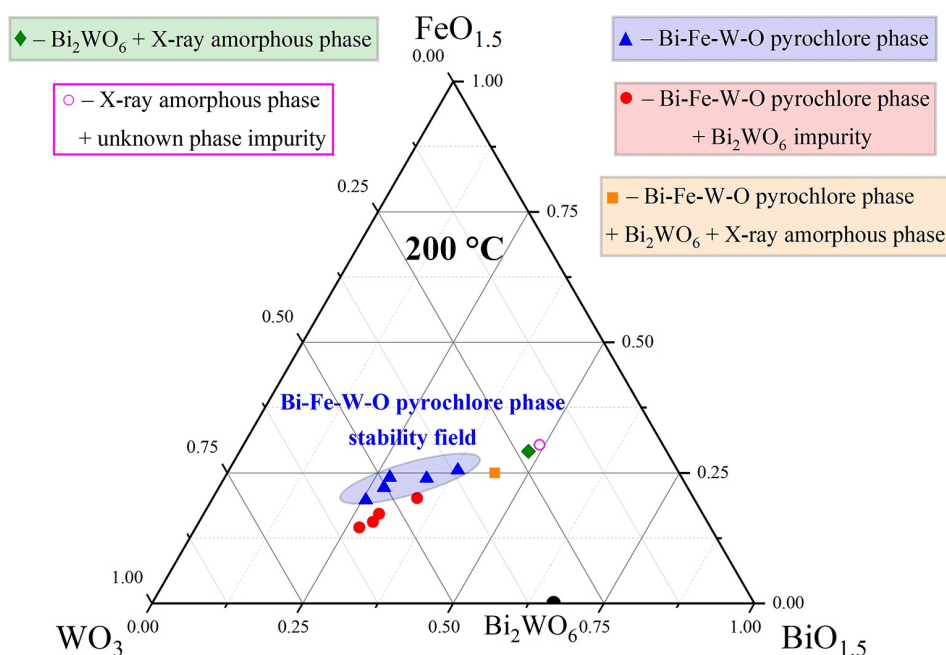


FIG. 6. Comparison of the bulk chemical composition and phase composition of the samples synthesized by the hydrothermal method on the concentration triangle of the $\text{BiO}_{1.5}\text{-FeO}_{1.5}\text{-WO}_3$ system (the shaded area indicates the localization of the pyrochlore-structured compounds concentration stability field at $T = 200^\circ\text{C}$)

3.3. SEM

The SEM data for the samples synthesized by the hydrothermal method are shown in Fig. 7 ((a) 5.6, (b) 5.8, (c) 5.9, (d) 5.16, (e) 5.12 and (f) 5.17). In samples 5.3 (not shown), 5.6, 5.8, 5.9 and 5.16, the only crystalline phase in which, according to the XRD data, is the pyrochlore phase, submicron particles of only one morphological motif are observed.

In sample 5.6, the particles have an almost spherical shape, resembling a poorly faceted octahedron, while in samples 5.3 (not shown), 5.8, 5.9 and 5.16 the particles have a predominantly clear octahedral shape. The octahedral morphology of the pyrochlore phase particles is determined by their synthesis conditions, mainly by the *pH* value of the hydrothermal fluid ($\text{pH} \sim 4\text{--}5$), as shown in [20].

In sample 5.12, in addition to the pyrochlore phase particles, which make up the bulk of the sample, rare plate-like particles with a thickness of $\sim 50\text{--}100$ nm are observed, fused with each other along flat edges into layered aggregates (Bi_2WO_6 phase). For other samples also containing impurity amounts of the Bi_2WO_6 phase (5.20, 5.21 and 5.22), a similar situation is observed, while micrographs of sample 5.17 are different, despite the qualitatively identical phase composition, according to XRD data.

Three morphological motifs are observed in micrographs of sample 5.17: (1) pyrochlore phase octahedral particles; (2) rod-shaped nanoparticles, which are, apparently, compounds with the Aurivillius phase structure; (3) agglomerates of nanoparticles, the morphology of which is difficult to determine according to SEM data. Since the reflections belonging to only two crystalline phases were detected in the XRD pattern of sample 5.17, the (3) nanoparticles observed in micrographs are apparently X-ray amorphous. Precise determination of the crystalline pyrochlore phase and Aurivillius phase individual particles composition in this sample employing the local EDXMA is complicated by the fact that the above-mentioned X-ray amorphous nanoparticles are localized, including on their surface. In micrographs of sample 5.18 (not shown), a similar situation is observed, but the pyrochlore phase particles are not detected in this case, which is consistent with XRD data. In micrographs of sample 5.34 (not shown), in which, according to XRD data, barely noticeable reflections of an unknown phase are observed against the background of an amorphous halo, the entire array of particles is represented by agglomerates of X-ray amorphous nanoparticles. In order to determine the nature and size of these nanoparticles, as well as the structure of rod-shaped nanoparticles, samples 5.17 and 5.18 were studied by the TEM method.

3.4. TEM

The TEM data for the samples synthesized by the hydrothermal method are shown in Fig. 8: (a,b,c,d) – 5.17 and (e,f) – 5.18. Three morphological motifs are observed in sample 5.17, which can be correlated with the XRD data as follows: (1) large octahedral particles of submicron sizes are pyrochlore-structured compounds (Fig. 8a); (2) rod-shaped nanoparticles of various lengths having a thickness of $\sim 10\text{--}30$ nm are, most likely, compounds with the Aurivillius phase structure (Bi_2WO_6 , PDF-2 No. 73-1126) (Fig. 8a,b,c); (3) almost spherical nanoparticles, which size is about 10 nm, are an X-ray amorphous phase (Fig. 8a,b,c). In sample 5.18, only (2) and (3) morphological motifs can be observed, which, apparently, correlate with the results of XRD in a similar way (Fig. 8e). The above assumptions are confirmed when considering nanoparticles in the high resolution mode (HRTEM), as well as when studying them using electron diffraction.

In the HRTEM, the structure of rod-shaped nanoparticles resembles a layered structure formed by alternating atomic planes composed of various sorts of atoms, as indicated by the different brightness of the atomic planes and the different interplanar distance between them (Fig. 8c). The Bi_2WO_6 compound is the simplest member of the Aurivillius phases family, the structure of which can be represented as two alternating layers: a fluorite-like layer $\text{Bi}_2\text{O}_2^{2+}$ and a perovskite-like layer WO_4^{2-} , while the unit cell parameter c is ~ 16.43 Å. In the micrograph of a rod-shaped nanoparticle obtained in the HRTEM, exactly such a layered structure is observed (Fig. 8c). If the left side of the nanoparticle is considered, then the following sequence of atomic planes alternation can be noted: two adjacent atomic planes having the same brightness, the distance between which is less than the distance from any of them to the nearest neighboring, brighter atomic plane, form a fluorite-like layer $\text{Bi}_2\text{O}_2^{2+}$, while the brighter atomic plane is a perovskite-like layer WO_4^{2-} . When comparing the observed structure with the Bi_2WO_6 compound unit cell structure, the average value of the parameter $c \sim 16.33$ Å over several unit cells was determined. When considering the right side of the same nanoparticle, a similar structure is observed, however, in this case, the atomic planes that make up the fluorite-like layer $\text{Bi}_2\text{O}_2^{2+}$ are brighter than the atomic plane, which is the perovskite-like layer WO_4^{2-} . The measured in this case average value of parameter c was ~ 16.07 Å over several unit cells. Similar measurements made for another rod-shaped nanoparticle (not shown) give a result close to the previous ones ~ 16.59 Å. When averaging all measured values of the unit cell parameter c , its value is ~ 16.33 Å, which indicates the formation of a single-layer Bi_2WO_6 phase and does not confirm an increase in the number of layers of the perovskite-like block. It should be noted that the rod-shaped nanoparticles observed in sample 5.18 have a similar structure and are the Bi_2WO_6 compound.

In Fig. 8c, in addition to the rod-shaped nanoparticle, several almost spherical nanoparticles can be noted, the size of which is about 10 nm. For nanoparticles that are found in the Bragg position, it is possible to observe sets of atomic planes that have the same brightness and a single interplanar distance within a particle. This, firstly, indicates the crystalline nature of such nanoparticles and, secondly, suggests that they are not layered compounds. In the electron diffraction pattern obtained from a certain group of such nanoparticles (Fig. 8d), the set of diffraction rings can be observed, while a broadened ring from the amorphous phase is not observed, which indicates the absence of an amorphous component.

In Fig. 8e (sample 5.18), a certain number of rod-shaped (Bi_2WO_6 compound) and almost spherical (X-ray amorphous phase) nanoparticles can be observed, the electron diffraction pattern from which is shown in Fig. 8f. When

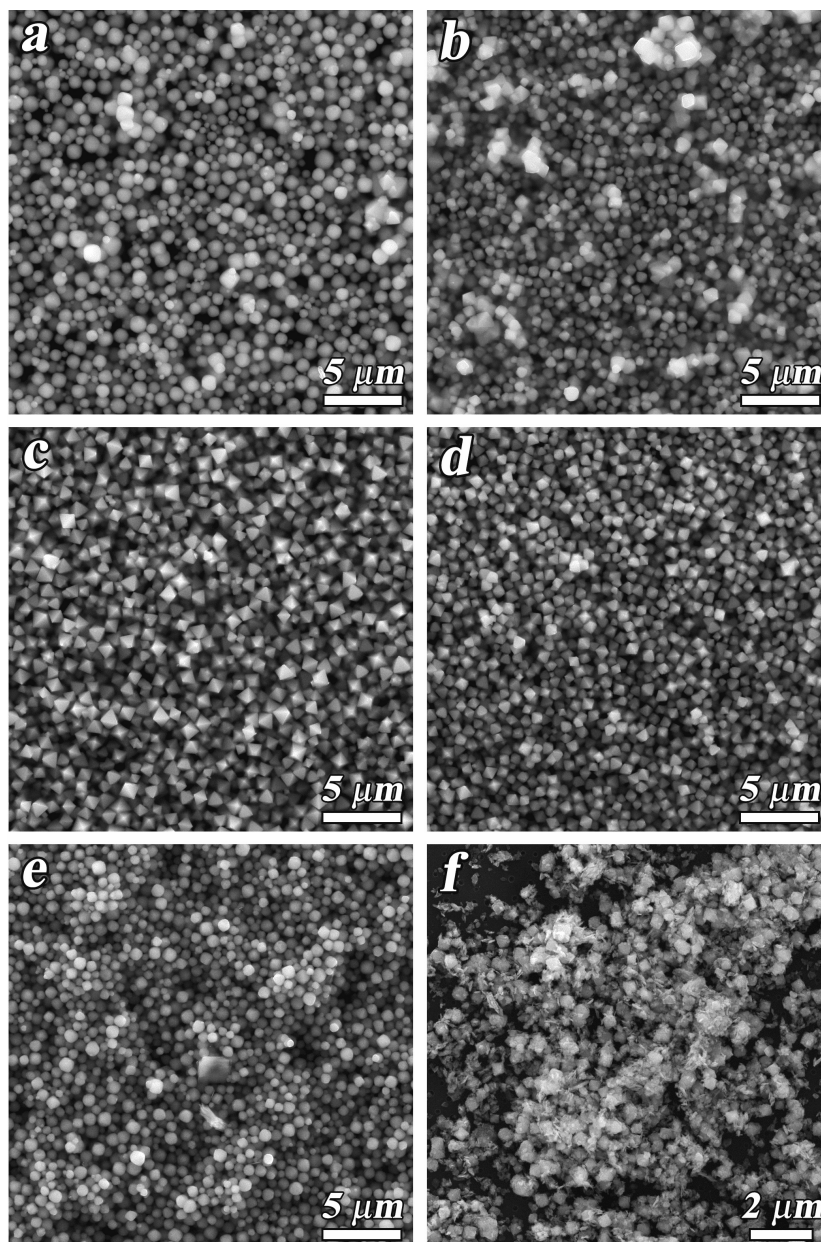


FIG. 7. SEM images of samples synthesized by the hydrothermal method: (a) 5.6, (b) 5.8, (c) 5.9, (d) 5.16, (e) 5.12 and (f) 5.17)

comparing the interplanar distances calculation results with a characteristic set of those for the Bi_2WO_6 compound, it was possible to establish a reliable match for eight of the ten indicated in Fig. 8f diffraction rings (Table 3). Two diffraction rings (3 and 10), the appearance of which is slightly different from the others, relate to diffraction from the substrate. It is not possible to perform a precise calculation of interplanar distances using other diffraction rings, that not indicated in Fig. 8f, due to their low brightness. It is important to note that the diffraction rings attributed to the Bi_2WO_6 compound may also relate to diffraction from nanoparticles of the X-ray amorphous phase, as well as other less bright and therefore not indicated in Fig. 8f diffraction rings.

3.5. Thermal stability

The thermal stability of the pyrochlore-structured compounds synthesized by the hydrothermal method was studied using sample 5.16 as an example. Two kinetic regimes were studied: (1) nonequilibrium (HTXRD and DSC/TG) and (2) quasi-equilibrium (annealing-quenching).

The data of the HTXRD of sample 5.16 (Fig. 9) indicate that no phase transformations occur in the sample up to a temperature of 545°C . Starting with a temperature of 585°C , the appearance of reflections belonging to the compound Bi_2WO_6 (PDF-2 No. 73-1126) is observed in HTXRD patterns. With a further increase in temperature to 765°C , the intensities of the Bi_2WO_6 phase reflections constantly increase, however, the pyrochlore-structured compound remains

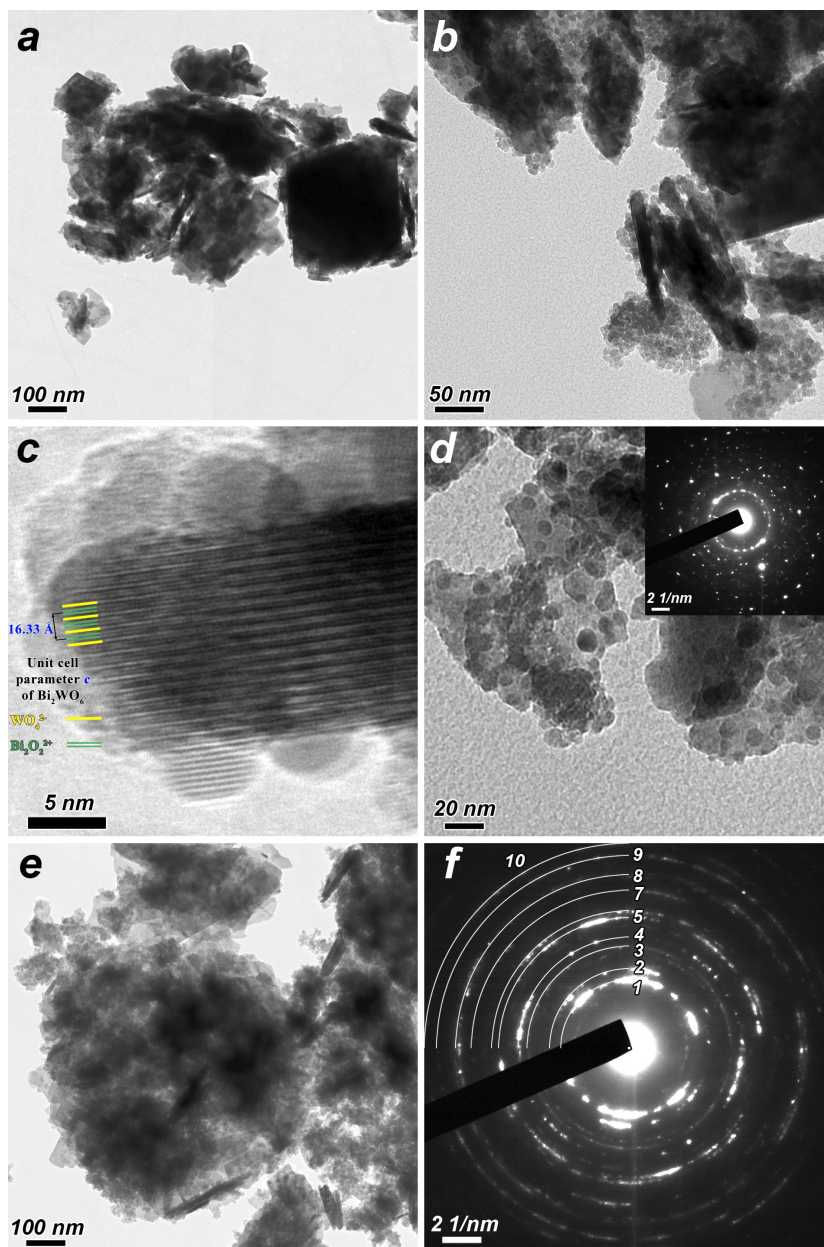


FIG. 8. TEM images of samples synthesized by the hydrothermal method: (a, b, c, d) 5.17 and (e, f) 5.18

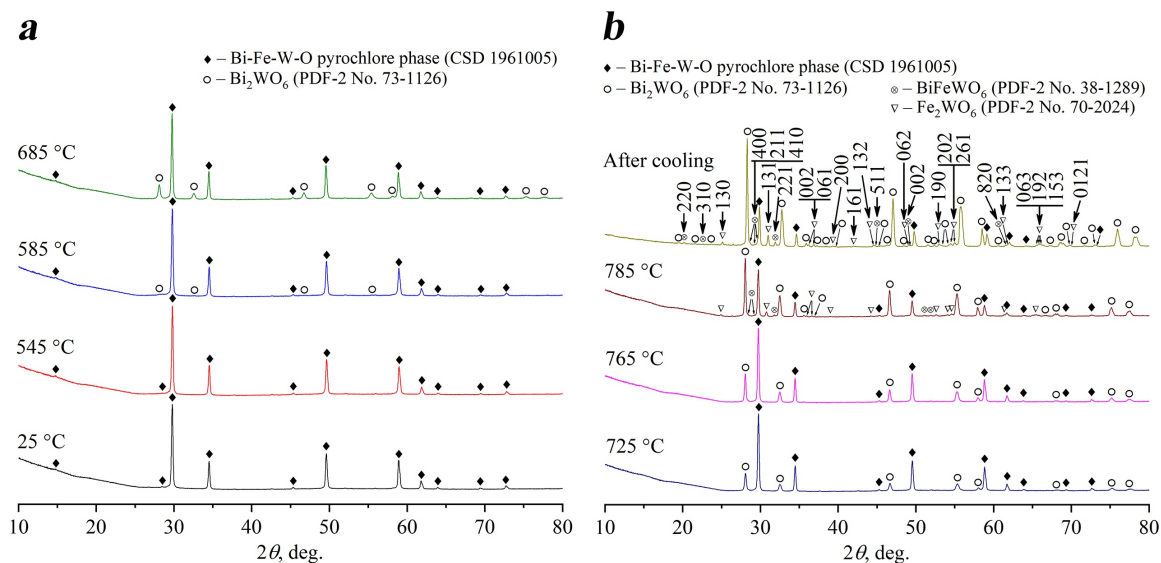
the predominant phase. The pyrochlore phase unit cell parameter increases in the temperature range 585–765°C, however, its change with increasing temperature is due not only to thermal lattice expansion, but also to a change in the composition of the compound during its gradual decomposition. At a temperature of 785°C, qualitative and significant quantitative changes can be noted in the HTXRD pattern: reflections of two new phases appear – Fe_2WO_6 (PDF-2 No. 70-2024) and BiFeWO_6 (PDF-2 No. 38-1289), and the amount of pyrochlore phase decreases sharply relative to the Bi_2WO_6 phase. No qualitative changes are observed in the XRD pattern obtained after cooling the sample from 785°C to room temperature in the natural mode (40–50 min), however, a further decrease in the amount of the pyrochlore phase is clearly noticeable compared to the amounts of Bi_2WO_6 , Fe_2WO_6 and BiFeWO_6 phases.

The presented results of HTXRD studies of sample 5.16 allow to conclude that in the temperature range 585–765°C the equilibrium composition of the pyrochlore phase changes, which corresponds to its continuous decomposition with the formation of the Bi_2WO_6 phase with an increase in temperature, while at a temperature of 785°C instantaneous decomposition of the pyrochlore phase of the composition corresponding to the higher temperature point of the pyrochlore stability field is observed.

The DSC/TG data for sample 5.16 are presented in Fig. 10. At the initial stage of heating in the range from 75°C to 230°C, a weak endothermic effect is observed on the DSC curve with a maximum at 130°C, which corresponds to a noticeable weight decrease of 1.37% on the TG curve. With further heating, weight loss is observed up to a temperature of 580°C, however, in the range of 230–580°C it proceeds more slowly and amounts to only 0.47%. Apparently, the

TABLE 3. The results of comparing the interplanar distances calculated from electron diffraction data with those for the Bi_2WO_6 compound (PDF-2 No. 73-1126)

The designation in Fig. 8f	Interplanar distances (d) according to the electron diffraction data (Fig. 8f), Å	Miller indices hkl of Bi_2WO_6 compound reflections
1	3.132	113
2	2.704	006 200 020
3	2.101	substrate
4	1.911	206 026 220 018
5	1.635	119 313 208 133
6	1.553	226 0110 218
7	1.353	0012 400 040 038
8	1.209	145 2012 0212 406 420 046 0310 240 238
9	1.103	2212 426 246 2310
10	1.036	substrate

FIG. 9. Powder XRD patterns of sample 5.16, measured *in situ* at various heating temperatures: (a) from 25 °C to 685 °C; (b) from 725 °C to 785 °C and after cooling from 785 °C to room temperature in the natural mode (Cu-K_α radiation) (Miller indices hkl are indicated only for selected reflections)

loss of weight at this stage of heating is due to further water removal, but decomposition of impurity carbonates formed during the hydrothermal synthesis is also possible. Further, when the sample is heated to a temperature of 815 °C, its mass practically does not change. On the DSC curve in the range from 230 °C to 795 °C, it is not possible to distinguish thermal effects due to their low intensity. According to the data of HTXRD analysis (Fig. 9), the pyrochlore phase decomposition occurs in the temperature range of 585–785 °C. This process, like most solid-phase reactions, is kinetically hindered and has small thermal effects, which makes it much more difficult to detect on the DSC curve. In the temperature range of 795–900 °C, three consecutive endothermic effects are observed, which can be associated with the melting of the phases formed during the pyrochlore phase decomposition.

Sample 5.16 was annealed sequentially to temperatures of 585 °C, 685 °C and 725 °C (Fig. 11), and quenching was carried out to room temperature in air by removing the crucible with the sample from a hot furnace. The duration of each annealing was 12 h, and the duration of cooling of the samples to room temperature was ~ 10–15 min. The sample obtained by annealing to a temperature of 585 °C, after XRD analysis, was used for annealing to a temperature of 685 °C

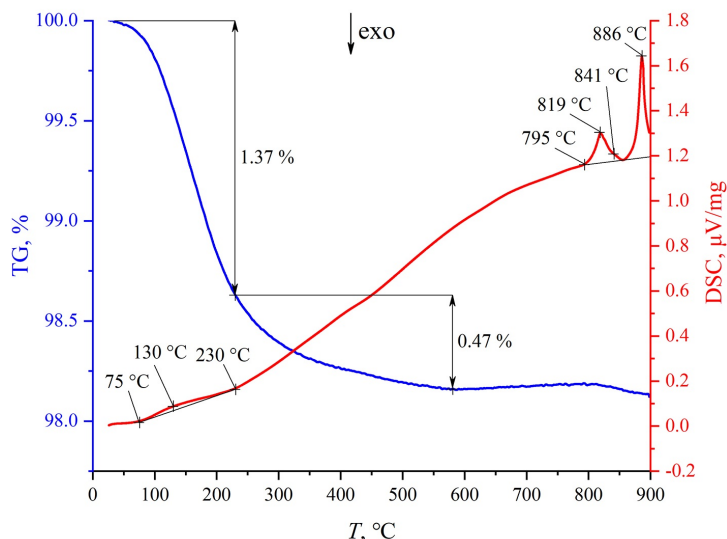


FIG. 10. DSC/TG curves obtained by heating the sample 5.16

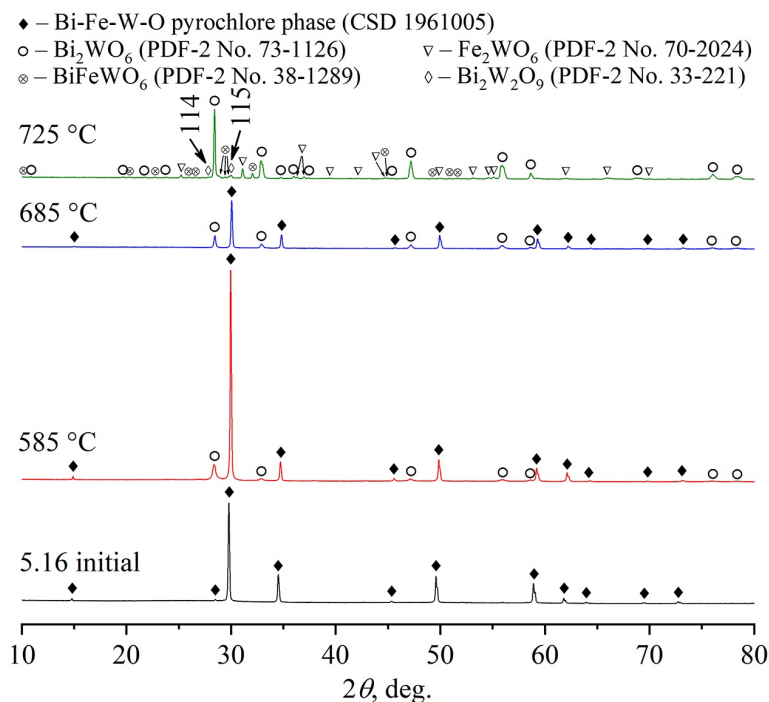


FIG. 11. Powder XRD patterns of samples obtained by annealing sample 5.16 to various temperatures (585°C, 685°C, and 725°C) with quenching to room temperature. The measurements were carried out at room temperature (Cu- K_{α} radiation) (Miller indices hkl are indicated only for selected reflections)

and so on. The bulk chemical compositions of the samples obtained as a result of annealing-quenching correspond within the limits of e.s.d.s to the initial sample composition, which indicates the absence of noticeable volatilization of the components.

In the XRD pattern of the sample obtained by annealing to 585°C, the appearance of the nanocrystalline Bi₂WO₆ (PDF-2 No. 73-1126) phase reflections is observed. The Aurivillius phase Bi₂WO₆ crystallite size in the crystallographic direction [113] was calculated using the Scherrer method and amounted to ~ 28 nm, however, the intensity of its reflections turns out to be several times greater than observed according to HTXRD data at this temperature (Fig. 9a,11). In the XRD pattern of the sample obtained by annealing to 685°C (Fig. 11), a further increase in the Bi₂WO₆ phase reflections intensity can be noted, which is qualitatively consistent with the HTXRD data (Fig. 9). Significant qualitative and quantitative changes are observed in the XRD pattern of the sample obtained by annealing to 725°C: the appearance of three new phases is recorded – Fe₂WO₆ (PDF-2 No. 70-2024), BiFeWO₆ (PDF-2 No. 38-1289) and barely noticeable amounts

of $\text{Bi}_2\text{W}_2\text{O}_9$ (PDF-2 No. 33-221), and the reflections of the pyrochlore phase are not observed, which indicates the completed decomposition of the pyrochlore phase having the composition corresponding to the higher temperature point of its stability field. Comparing the phase composition of the sample obtained by annealing to 725°C and the HTXRD data obtained in the temperature range $725\text{--}785^\circ\text{C}$ (Fig. 9b,11), it can be concluded that the temperature readings when recording the XRD pattern *in situ* are more than 60°C ahead of the temperature at which the phase composition observed on the HTXRD is equilibrium.

4. Conclusions

Pyrochlore-structured compounds of variable composition formed in the $\text{Bi}_2\text{O}_3\text{--Fe}_2\text{O}_3\text{--WO}_3$ system under hydrothermal conditions ($T = 200^\circ\text{C}$, $P = 7$ MPa, hydrothermal fluid $\text{pH} \sim 4\text{--}5$) were obtained in the form of single-phase materials and as part of composite nanomaterials, and characterized.

The concentration stability field localization of the pyrochlore-structured compounds was established and phase equilibria involving these compounds were studied. It was shown that under the studied hydrothermal synthesis conditions, a pyrochlore-structured compounds were obtained in the form of submicron particles, predominantly of a clear octahedral shape, which indicates the intensification of their growth processes under such conditions. At the same time, it was found that the phases coexisting with these compounds are formed in nanocrystalline form: in the region of two-phase equilibrium from the $\text{Bi}_2\text{O}_3\text{--WO}_3$ system side, plate-like (thickness $h \sim 50\text{--}100$ nm) nanoparticles of the Bi_2WO_6 compound are formed; in the region of compositions from the $\text{Bi}_2\text{O}_3\text{--Fe}_2\text{O}_3$ system side, rod-shaped ($h \sim 10\text{--}30$ nm) nanoparticles of the Bi_2WO_6 compound are formed, which crystallite size in the crystallographic direction [113] is ~ 20 nm, as well as X-ray amorphous nanoparticles with a size of about 10 nm.

The presented results of pyrochlore-structured compounds thermal stability investigation allow to conclude that in the temperature range from $\sim 585^\circ\text{C}$ to $\sim 725^\circ\text{C}$ the equilibrium composition of the pyrochlore phase changes, which corresponds to its continuous decomposition with the formation of the nanocrystalline Bi_2WO_6 phase with an increase in temperature, while at a temperature of 725°C instantaneous decomposition of the pyrochlore phase of the composition corresponding to the higher temperature point of the pyrochlore stability field is observed.

References

- [1] Ellert O.G., Egorysheva A.V., Gajtko O.M., Kirdyankin D.I., Svetogorov R.D. Highly Frustrated Bi–Cr–Sb–O Pyrochlore with Spin-Glass Transition. *Journal of Magnetism and Magnetic Materials*, 2018, **463**, P. 13–18.
- [2] Egorysheva A.V., Ellert O.G., Maksimov Y.V., Volodin V.D., Efimov N.N., Novotortsev V.M. Subsolidus Phase Equilibria and Magnetic Characterization of the Pyrochlore in the $\text{Bi}_2\text{O}_3\text{--Fe}_2\text{O}_3\text{--Sb}_2\text{O}_x$ System. *Journal of Alloys and Compounds*, 2013, **579**, P. 311–314.
- [3] Koroleva M.S., Piir I.V., Ryabkov Yu.I., Korolev D.A., Chezhina N.V. Synthesis and Properties of Chromium-Containing Bismuth Titanates with the Pyrochlore Structure. *Russian Chemical Bulletin, International Edition*, 2013, **62**(2), P. 408–411.
- [4] Babu G.S., Bedanta S., Valant M. Evidence of the spin glass state in $(\text{Bi}_{1.88}\text{Fe}_{0.12})(\text{Fe}_{1.42}\text{Te}_{0.58})\text{O}_{6.87}$ pyrochlore. *Solid State Communications*, 2013, **158**, P. 51–53.
- [5] Lufaso M.W., Vanderah T.A., Pazos I.M., Levin I., Roth R.S., Nino J.C., Provenzano V., Schenck P.K. Phase Formation, Crystal Chemistry, and Properties in the System $\text{Bi}_2\text{O}_3\text{--Fe}_2\text{O}_3\text{--Nb}_2\text{O}_5$. *Journal of Solid State Chemistry*, 2006, **179**(12), P. 3900–3910.
- [6] Jusoh F.A., Tan K.B., Zainal Z., Chen S.K., Khaw C.C., Lee O.J. Novel pyrochlores in the $\text{Bi}_2\text{O}_3\text{--Fe}_2\text{O}_3\text{--Ta}_2\text{O}_5$ (BFT) Ternary System: Synthesis, Structural and Electrical Properties. *Journal of Materials Research and Technology*, 2020, **9**(5), P. 11022–11034.
- [7] Liu W., Wang H. Enhanced Dielectric Properties of $\text{Bi}_{1.5}\text{ZnNb}_{1.5}\text{O}_7$ Thick Films via Cold Isostatic Pressing. *Journal of Electroceramics*, 2012, **29**(3), P. 183–186.
- [8] Piir I.V., Koroleva M.S., Ryabkov Y.I., Korolev D.A., Chezhina N.V., Semenov V.G., Panchuk V.V. Bismuth Iron Titanate Pyrochlores: Thermostability, Structure and Properties. *Journal of Solid State Chemistry*, 2013, **204**, P. 245–250.
- [9] Krasnov A.G., Piir I.V., Koroleva M.S., Sekushin N.A., Ryabkov Y.I., Piskaykina M.M., Sadykov V.A., Sadovskaya E.M., Pelipenko V.V., Ereemeev N.F. The Conductivity and Ionic Transport of Doped Bismuth Titanate Pyrochlore $\text{Bi}_{1.6}\text{M}_x\text{Ti}_2\text{O}_{7-\delta}$ ($M\text{--Mg, Sc, Cu}$). *Solid State Ionics*, 2017, **302**, P. 118–125.
- [10] Egorysheva A.V., Gajtko O.M., Rudnev P.O., Ellert O.G., Ivanov V.K. Synthesis of Bi–Fe–Sb–O Pyrochlore Nanoparticles with Visible-Light Photocatalytic Activity. *European Journal of Inorganic Chemistry*, 2016, **13–14**, P. 2193–2199.
- [11] Bencina M., Valant M., Pitcher M.W., Fanetti M. Intensive Visible-Light Photoactivity of Bi- and Fe-Containing Pyrochlore Nanoparticles. *Nanoscale*, 2014, **6**(2), P. 745–748.
- [12] Allured B., Delacruz S., Darling T., Huda M.N., Subramanian V.(R.) Enhancing the visible light absorbance of $\text{Bi}_2\text{Ti}_2\text{O}_7$ through Fe-substitution and its effects on photocatalytic hydrogen evolution. *Appl. Catal. B Environ.*, 2014, **144**, P. 261–268.
- [13] Pyrochlorine Materials and thermal barrier coating with these pyrochlore materials, Patent. 2454477 Russia: MPK C22C 29/12, C23C 30/00, Malov T., Oexchep M., N 2009116606/02, Issue N 18, 27.06.2012.
- [14] Xue J., Zhang K., He Z., Zhao W., Li W., Xie D., Luo B., Xu K., Zhang H. Rapid Immobilization of Simulated Radioactive Soil Waste Using Self-Propagating Synthesized $\text{Gd}_2\text{Ti}_2\text{O}_7$ Pyrochlore Matrix. *Materials*, 2019, **12**(7), P. 1163.
- [15] Benčina M., Valant M. $\text{Bi}_2\text{Ti}_2\text{O}_7$ -based pyrochlore nanoparticles and their superior photocatalytic activity under visible light. *Journal of the American Ceramic Society*, 2017, **101**(1), P. 82–90.
- [16] Castellano C., Berti G., Rubio-Marcos F., Lamura G., Sanna S., Salas-Colera E., Brambilla A., Muñoz-Noval Á., Duò L., Demartin F. Anomalous local lattice disorder and distortion in $\text{A}_2\text{Mo}_2\text{O}_7$ pyrochlores. *Journal of Alloys and Compounds*, 2017, **723**, P. 327–332.
- [17] Zhuk N.A., Krzhizhanovskaya M.G., Koroleva A.V., Semenov V.G., Selyutin A.A., Lebedev A.M., Nekipelov S.V., Sivkov D.V., Kharton V.V., Lutoev V.P., Makeev B.A. Fe,Mg-Codoped Bismuth Tantalate Pyrochlores: Crystal Structure, Thermal Stability, Optical and Electrical Properties, XPS, NEXAFS, ESR, and ^{57}Fe Mössbauer Spectroscopy Study. *Inorganics*, 2023, **11**(1), P. 8.
- [18] Guskov V.N., Gagarin P.G., Tyurin A.V., Khoroshilov A.V., Guskov A.V., Gavrichev K.S. Heat capacity of solutions $\text{LaLnZr}_2\text{O}_7$ ($\text{Ln} = \text{Sm, Gd, Dy}$) with the structure of pyrochlore in the temperature range of $10\text{--}1400$ K. *Russian Journal of Physical Chemistry A*, 2020, **94**(2), P. 233–239.

- [19] Lomakin M.S., Proskurina O.V., Gusarov V.V. Pyrochlore phase in the $\text{Bi}_2\text{O}_3\text{-Fe}_2\text{O}_3\text{-WO}_3\text{-(H}_2\text{O)}$ system: its formation by hydrothermal synthesis in the low-temperature region of the phase diagram. *Nanosystems: Phys. Chem. Math.*, 2023, **14**(2), P. 242–253.
- [20] Lomakin M.S., Proskurina O.V., Levin A.A., Sergeev A.A., Leonov A.A., Nevedomskiy V.N., Voznesenskiy S.S. Pyrochlore Phase in the $\text{Bi}_2\text{O}_3\text{-Fe}_2\text{O}_3\text{-WO}_3\text{-(H}_2\text{O)}$ System: its Formation by Hydrothermal-Microwave Synthesis and Optical Properties. *Russ. J. Inorg. Chem.* 2022, **67**(6), P. 820–829.
- [21] Lomakin M.S., Proskurina O.V., Abiev R.Sh., Nevedomskiy V.N., Leonov A.A., Voznesenskiy S.S., Gusarov V.V. Pyrochlore phase in the $\text{Bi}_2\text{O}_3\text{-Fe}_2\text{O}_3\text{-WO}_3\text{-(H}_2\text{O)}$ system: physicochemical and hydrodynamic aspects of its production using a microreactor with intensively swirled flows. *Advanced Powder Technology*, 2023, **34**(7), 104053.
- [22] Daniels L.M., Playford H.Y., Grenèche J.-M., Hannon A.C., Walton R.I. Metastable $(\text{Bi}, M)_2(\text{Fe}, \text{Mn}, \text{Bi})_2\text{O}_{6+x}$ ($M = \text{Na}$ or K) Pyrochlores from Hydrothermal Synthesis. *Inorganic Chemistry*, 2014, **53**(24), P. 13197–13206.
- [23] Egorysheva A.V., Gajtko O.M., Rudnev P.O., Ellert O.G., Ivanov V.K. Synthesis of Bi–Fe–Sb–O Pyrochlore nanoparticles with visible-light photocatalytic activity. *Eur. J. Inorg. Chem.*, 2016, **13–14**, P. 2193–2199.
- [24] Radha R., Srinivasan A., Manimuthu P., Balakumar S. Tailored sunlight driven nano-photocatalyst: bismuth iron tungstate (BiFeWO_6), *J. Mater. Chem. C*, 2015, **3**(39), P. 10285–10292.
- [25] Annamalai K., Radha R., Vijayakumari S., Kichanov S.E., Balakumar S. Insight into the investigation on nanostructured defect pyrochlore $\text{Bi}_{2-x}\text{Fe}_x\text{WO}_6$ and its photocatalytic degradation of mixed cationic dyes. *Materials Science in Semiconductor Processing*, 2022, **150**, 2022, P. 106961.
- [26] Wang Y., Zhang S., Zhong Q., Zeng Y., Ou M., Cai W. Hydrothermal synthesis of novel uniform nanooctahedral $\text{Bi}_3(\text{FeO}_4)(\text{WO}_4)_2$ solid oxide and visible-light photocatalytic performance. *Ind. Eng. Chem. Res.*, 2016, **55**(49), P. 12539–12546.
- [27] Lomakin M.S., Proskurina O.V., Danilovich D.P., Panchuk V.V., Semenov V.G., Gusarov V.V. Hydrothermal Synthesis, Phase Formation and Crystal Chemistry of the pyrochlore/ Bi_2WO_6 and pyrochlore/ $\alpha\text{-Fe}_2\text{O}_3$ Composites in the $\text{Bi}_2\text{O}_3\text{-Fe}_2\text{O}_3\text{-WO}_3$ System. *J. Solid State Chem.*, 2020, **282**, P. 121064.
- [28] Narykova M.V., Levin A.A., Prasolov N.D., Lihachev A.I., Kardashev B.K., Kadomtsev A.G., Panfilov A.G., Sokolov R.V., Brunkov P.N., Sultanov M.M., Kuryanov V.N., Tyshkevich V.N. The structure of the near-surface layer of the AAAC overhead power line wires after operation and its effect on their elastic, microplastic, and electroresistance properties. *Crystals*, 2022, **12**, P. 166.
- [29] Fawcett T.G., Kabekkodu S.N., Blanton J.R., Blanton T.N. Chemical analysis by diffraction: the Powder Diffraction File™. *Powder Diffr.*, 2017, **32**, P. 63–71.
- [30] Maunders C., Etheridge J., Wright N., Whitfield H.J. Structure and microstructure of hexagonal $\text{Ba}_3\text{Ti}_2\text{RuO}_9$ by electron diffraction and microscopy. *Acta Crystallogr. B.*, 2005, **61**, P. 154–159.
- [31] Levin A.A. Program *SizeCr* for calculation of the microstructure parameters from X-ray diffraction data. preprint ResearchGate, 2022.
- [32] Terlan B., Levin A.A., Börrnert F., Simon F., Oschatz M., Schmidt M., Cardoso-Gil R., Lorenz T., Baburin I.A., Joswig J.-O., Eychmüller A. Effect of Surface Properties on the Microstructure, Thermal, and Colloidal Stability of VB_2 Nanoparticles. *Chem. Mater.*, 2015, **27**, P. 5106–5115.
- [33] Terlan B., Levin A.A., Börrnert F., Zeisner J., Kataev V., Schmidt M., Eychmüller A. A Size-Dependent Analysis of the Structural, Surface, Colloidal, and Thermal Properties of $\text{Ti}_{1-x}\text{B}_2$ ($x = 0.03\text{--}0.08$) Nanoparticles. *Eur. J. Inorg. Chem.*, 2016, **6**, P. 3460–3468.
- [34] Langford L., Cernik R. J., Louer D. The Breadth and Shape of Instrumental Line Profiles in High-Resolution Powder Diffraction. *J. Appl. Phys.*, 1991, **24**, P. 913–919.
- [35] Scherrer P. Bestimmung der Grösse und der inneren Struktur von Kolloidteilchen mittels Röntgenstrahlen. *Nachr. Königl. Ges. Wiss. Göttingen.*, 1918, **26**, P. 98–100. (in German)
- [36] Stokes A.R., Wilson A.J.C. The diffraction of X-rays by distorted crystal aggregates. *Proc. Phys. Soc. London*, 1944, **56**, P. 174–181.

Submitted 26 October 2023; revised 20 November 2023; accepted 5 December 2023

Information about the authors:

Makariy S. Lomakin – Ioffe Institute, 26, Politekhnicheskaya St., 194021, St. Petersburg, Russia; St. Petersburg Electrotechnical University “LETI”, 5, Professor Popov St., 197376, St. Petersburg, Russia; ORCID 0000-0001-5455-4541; lomakinmakariy@gmail.com

Olga V. Proskurina – Ioffe Institute, 26, Politekhnicheskaya St., 194021, St. Petersburg, Russia; St. Petersburg State Institute of Technology, 26, Moskovsky Ave., 190013, St. Petersburg, Russia; ORCID 0000-0002-2807-375X; proskuri-naov@mail.ru

Aleksandr A. Levin – Ioffe Institute, 26, Politekhnicheskaya St., 194021, St. Petersburg, Russia; ORCID 0000-0001-9258-3204; aleksandr.a.levin@mail.ioffe.ru

Vladimir N. Nevedomskiy – Ioffe Institute, 26, Politekhnicheskaya St., 194021, St. Petersburg, Russia; ORCID 0000-0002-7661-9155; nevedom@mail.ioffe.ru

Conflict of interest: the authors declare no conflict of interest.